This is a preprint, the final version is subject to change, of the American Mineralogist (MSA)
Cite as Authors (Year) Title. American Mineralogist, in press.
(DOI will not work until issue is live.) DOI: http://dx.doi.org/10.2138/am-2016-5605

Revision 1

What is the actual structure of samarskite-(Y)? A TEM investigation of metamict samarskite from the Garnet Codera dike pegmatite (Central Italian Alps).

Gian Carlo Capitani[1*], Enrico Mugnaioli[2], Alessandro Guastoni[3]

[1] Department of Earth and Environmental Sciences, University of Milano-Bicocca, Italy

[2] Department of Physical Sciences, Earth and Environment, University of Siena, Italy

[3] Department of Geoscience, University of Padova, Italy

*corresponding author: giancarlo.capitani@unimib.it

Key words: samarskite-(Y), niobioaeschynite-(Y), TEM, electron diffraction tomography.

Abstract

(Y-REE-U-Th)-(Nb-Ta-Ti) oxides from the Garnet Codera dike pegmatite (Central Italian Alps), with compositions in the samarskite-(Y) field and that gave amorphous response at the single crystal X-ray diffractometer, were investigated by scanning and transmission electron microscopy (SEM, TEM), wavelength and energy dispersive spectroscopy (WDS, EDS), and electron diffraction tomography (EDT).

Back-scattered electron images reveal that the samples are zoned with major substitutions involving (U + Th) with respect to (Y + REE). At the TEM scale, the samples show a continuous range of variability both in terms of composition and in radiation damage, and the amount of radiation damage is directly

correlated with the U-content. Areas with high U-content and highly damaged show crystalline, randomly oriented nanoparticles that are interpreted as decomposition products of the metamictization process. On the other hand, areas with lower U-content and radiation dose contained within $0.7 \cdot 10^{16}$ α-event/mg, although severely damaged, still preserve single crystal appearance. Such areas, noticeably consisting of relicts of the original samarskite structure, were deeply investigated by electron diffraction techniques. Surprisingly, the retrieved crystal structure of untreated samarskite is consistent with aeschynite and not with ixiolite (or columbite), as believed so far after X-ray diffraction experiments on annealed samples. In particular, the resolved structure is a niobioaeschynite-(Y), with *Pnma* space group, cell parameters a = 10.804(1), b = 7.680(1), c = 5.103(1) Å, and composition $(Y_{0.53}Fe_{0.22}Ca_{0.10}U_{0.09}Mn_{0.07})_{\Sigma=1}(Nb_{1.07}Ti_{0.47}Fe_{0.34}Ta_{0.07}W_{0.06})_{\Sigma=2}O_6$. If this finding can be confirmed and extended to the other members of the group (namely samarskite-(Yb), calciosamarskite, and ishikawaite), then the samarskite mineral group should be considered no longer as an independent mineral group but as part of the aeschynite group of minerals.

It is finally suggested that the rare crystalline sub-micrometric ixiolite domains, occasionally spotted in the sample by TEM, or the nanoparticles detected in highly metamict areas interpreted as decomposition product of the metamictization process, which may have in fact the ixiolite structure, act as seeds during annealing, leading to the detection of ixiolite peaks in the X-ray powder diffractograms.

Introduction

Most niobium-tantalum-titanium oxide minerals, common accessory minerals of granitic pegmatites, contain yttrium, rare earths, iron and manganese, together with relatively high amounts of radioactive elements such as uranium and thorium, whose decay causes their structure to become metamict over geological times. As a consequence, the identification of these minerals is not trivial, since many of them

are so structurally compromised by radiation damage that their crystallographic determination is impossible. Other diagnostic features may be either not present (e.g., crystal forms, cleavage), common to several minerals (e.g., surface luster, color), or heavily altered by the metamictization process (e.g., birefrangence). As such, phase identification is commonly done on the basis of mineral-chemistry alone. However, especially for some oxide minerals where yttrium is the dominant metal, mineral identification via compositional data alone is often ambiguous, and over the time has given origin to confusion in their naming, systematics, and crystal chemistry (e.g., Ewing 1976; Ercit 2005; Škoda and Novák 2007). In fact, many diverse mineral groups show compositional overlapping, e.g., fergusonite versus samarskite and euxenite versus aeschynite. There are doubts about the proper cation site assignment, which is distinctive for some minerals, as well as about the knowledge of the valence state of iron and uranium, which is impossible to determine by electron microprobe, i.e. the most common analytical technique in mineral sciences. Moreover, the presence of additional, partially occupied sites that originate from the metamictization process, further complicate the task (Bonazzi and Menchetti 1999).

For these reasons, the identification of metamict minerals is usually done through X-ray diffraction of recovered material after heating and recrystallization at high temperature. Also in this case, however, several problems arise. First, the chemical composition of the metamict mineral may have experienced compositional changes, during geological times, due to infiltration of metasomatic fluids, which may find a preferential pathway and a more reactive exchange medium in the amorphous regions (e.g., Bonazzi et al. 2006). Second, the annealed material is usually polyphasic, due to the presence of crystalline inclusions in the metamict sample that act as seeds, and the related additional peaks complicate the interpretation of the powder diffraction pattern (e.g., Sugitani et al. 1984, Tomašić et al. 2010). Moreover, these additional phases withdraw from the system elements that become no longer available for the main phase, which may develop as a phase inconsistent with the original mineral.

In this paper, we employed transmission electron microscopy (TEM), energy dispersive spectroscopy

(EDS) and electron diffraction tomography (EDT) for characterizing a metamict mineral from the Garnet Codera dike pegmatite (Central Italian Alps), whose identification was doubtful after wavelength dispersive (WDS) electron microprobe (EMP) analyses and that was amorphous at the single crystal diffractometer. Nonetheless, as often observed for metamict minerals (e.g. Capitani et al. 2000; Bonazzi et al. 2006, 2009), the investigated sample shows nanosized domains coherently oriented which represent remnants of the original structure. Thanks to the strong interaction between accelerated electrons and matter, 10^3-10^4 times greater than for X-rays, small volumes of diffracting material are sufficient to collect instantaneously an electron diffraction pattern. It was therefore possible to collect from single nanosized domains punctual chemical analyses and 3D electron diffraction data sets that allowed *ab-inito* crystal structure determination and thus an unambiguous identification of the metamict sample as aeschynite-(Y).

The Codera Valley pegmatite

The studied (Y-REE-U-Th)-(Nb-Ta-Ti) oxides occur in a pegmatite named Garnet Codera pegmatite. This pegmatite belongs to swarms of pegmatite dikes cropping out along the ancient glacial circle located in the upper Codera Valley (Central Italian Alps) that intrude both the main granodiorite body and the outer thin tonalite rim of the Masino-Bregaglia pluton (Guastoni et al. 2014). Dikes were emplaced during the syn-magmatic stage above 500 °C, which was characterized by a pervasive solid-state foliation and circulation of late stage hydrothermal fluids. Crosscutting relationships indicate the presence of more than a single generation of pegmatite dikes. U-Th-Pb dating on monazite and xenotime indicate an average emplacement age of 25-26 Ma (Guastoni, unpublished data).

The Garnet Codera dike crops out for 30 meters, reaches up to 3 meters in width, and shows boudins and lobate structures along the contacts with the enclosing rocks. It shows symmetric core-border zoning in

terms of mineral assemblage, with the core composed by coarse-grained (pluridecimetric) vitreous smoky quartz and decimetric white K-feldspar perthite crystals. Both these minerals are elongated along the strike of the dike due to the effect of the intense ductile deformation that occurred during cooling. In the core zone, accessory minerals like red garnet and beryl "aquamarine" crystals are common. The wall-intermediate zone is mainly composed of K-feldspar and graphic quartz+K-feldspar textures are locally predominant. In this portion, granular black magnetite and layers of millimetric trapezohedral red spessartine are also present.

The border zone is composed by medium-grained (pluricentimetric) white K-feldspar, quartz, biotite flakes that developed comb textures. In this area, a number of REE-U bearing minerals were described, including (Y-REE-U-Th)-(Nb-Ta-Ti) oxides, uraninite, monazite-(Ce), and zircon (Guastoni et al. 2014). The (Y-REE-U-Th)-(Nb-Ta-Ti) oxides include columbite-(Fe), euxenite-(Y) and other compositionally related oxides, possibly belonging to the samarskite group minerals, whose definitive identification could not be ascertained due to their metamict state. These oxides occur as black to reddish-brown, platy or prismatic crystals, with conchoidal fracture and vitreous luster and up to 1 centimeter in length.

Samarskite and related (Y-REE-U-Th)-(Nb-Ta-Ti) oxides

The outstanding features of the (Y-REE-U-Th)-(Nb-Ta-Ti) oxides relevant for the present study are briefly reported below and summarized in Table 1. Aeschynite and euxenite groups have the general formula AB_2O_6, where A is 8-fold coordinated in a typical square antiprism and mostly occupied by Y, REE, Ca, and U, and B is 6-fold coordinated and mostly occupied by Ti, Nb, and Ta. Both structures are orthorhombic, but stacking of the BO_6 octahedra is different leading to the *Pbnm* space group in aeschynite and to the *Pbcn* space group in euxenite. In particular, in the aeschynite structure, pairs of

edge-sharing BO_6 octahedra are connected by corners to form double chains running in a zigzag pattern along the **b** axis (Aleksandrov 1962). In the euxenite structure, the BO_6 octahedra form double layers stacked parallel to the **c** axis, joined both by edge and corner-sharing (Weitzel and Schröcke, 1980). Annealing experiments on aeschynite-(Y) evidence the beginning of a phase transition towards euxenite at 800 °C (Bonazzi et al. 2002; Tomašić et al. 2004). The aeschynite structure shows a preference for larger A cations than the euxenite structure. Different aeschynite and euxenite mineral members are distinguished by the dominant A and B cations.

The currently accepted structural formula of samarskite is ABO_4, with A mostly occupied by Y, REE, Ca, U, Fe^{2+} and Fe^{3+}, and B mostly occupied by Ta, Nb and Ti. Iron is usually reported as a subordinate A cation, although some studies place Fe^{3+} in the B-site (Warner and Ewing 1993). All minerals of the samarskite group have Nb as dominant cation on the B-site, thus the different member of the group can be mutually distinguished by the dominant A-site cation (Hanson et al., 1999). The REE-dominant member is usually samarskite-(Y), even if an ytterbium-dominant samarskite-(Yb) has also been reported (Simmons et al., 2006). The member with uranium dominant at the A-site is ishikawaite, and the calcium-dominant one is calciosamarskite.

For none of these minerals the crystal structure has been thoughtfully described. According to the available data, a low-temperature samarskite modification and a high-temperature samarskite modification may be possible. On the basis of chemical composition, orthorhombic morphology preserved in rare euhedral samples (Palache et al., 1944), and X-ray diffraction (XRD) data on natural and synthetic samples annealed at 550 °C (Sugitani et al., 1984, 1985), the low-temperature modification is commonly assumed to have the columbite- or ixiolite-type structure and most likely crystallizes in *Pbcn* space group. The high-temperature samarskite is assumed to have the wolframite-type structure and space group *P*2/*c,* as revealed by XRD patterns of samples annealed at temperatures around 1000 °C (Komkov, 1965; Sugitani et al., 1985). Remarkably, only octahedral cation sites are present in ixiolite,

145 columbite, and wolframite, an arguably close packing for large radius elements like Y, REE, Th and U.

146

147 **Experimental methods**

148

149 Two mounts from the same U-bearing sample from the Garnet Codera dike were prepared for TEM-EDS
150 investigations. The crystal aggregates were embedded in epoxy, polished on one side, and carbon coated.
151 At this stage, samples were observed at the SEM with the aim to carry out a map to guide the further
152 preparation of the TEM foils. A Tescan Vega TS 5136XM SEM, equipped with an EDAX Genesis
153 4000XMS EDS system, made available at the Earth and Environmental Sciences Department of the
154 University of Milano-Bicocca, was used for this step. Spot analyses and compositional profiles were
155 acquired at 20 keV on specific microstructures evidenced by BSE images. The standardless method (i.e.,
156 theoretical K-factors) and the ZAF correction method was employed for semi-quantitative analysis.
157 Quantitative chemical composition of (Y-REE-U-Th)-(Nb-Ta-Ti) oxides were determined using a
158 Cameca-Camebax SX50 wavelength-dispersive electron microprobe at the University of Padova,
159 operating at 20 KeV with probe current of 20 nA and probe diameter of ~1 μm. Counting times were 10
160 s and 5 s at peak position and background for major elements, and 20 s and 10 s at peak position and
161 background for minor elements. X-ray counts were converted to oxide wt% using the PAP correction
162 program supplied by Cameca (Pouchou and Pichoir 1991). Peak overlaps within the REE were
163 minimized by using the *L*β peak position for Nd and *L*α peak positions for all the other elements. The
164 following natural and synthetic standards, spectral lines, and analyzing crystals were used: wollastonite
165 (Ca*K*α, TAP), MgO (Mg*K*α, TAP), $MnTiO_3$ (Mn*K*α, LiF), $ScPO_4$ (Sc*K*α, LiF), TiO_2 (Ti*K*α, TAP), Fe_2O_3
166 (Fe*K*α, LiF), Zr-Y-REE-silicates (Y*L*α, REE*L*α and Nd*L*β, LiF), synthetic UO_2 and ThO_2 (U*M*α and
167 Th*M*α, PET), metallic Nb (Nb*L*α, PET), and metallic Ta, Sn and W (Ta*L*α, Sn*L*α and W*L*α, LiF). In all
168 examined Nb-Ta oxides, the concentrations of Al, Zr, Ba, Pb, La, Ce were found to be below the limits of

169 detection (0.05 wt%), while Tb and Ho were not analyzed. Analytical precision is estimated to within 1%
170 for major elements and 5% for minor elements.
171 After this step, the two mounts were sectioned parallel to the polished surface with a diamond wheel,
172 mechanically milled down to 30 μm, polished on the rough side and then ion milled down to electron
173 transparency with a Gatan PIPS instrument made available at the Earth Science Department of the
174 University of Milan.
175 TEM investigations were performed at the Department of Physical Sciences, Earth and Environment of
176 the University of Siena with a Jeol JEM 2010 instrument operating at 200 keV and equipped with an
177 Oxford ISIS EDS system. Samples were first carbon coated to avoid charging during observation, and
178 later mounted on a JEOL double tilt holder. The standardless EDS method and the Cliff Lorimer
179 approximation (Cliff and Lorimer 1975) was employed for semi-quantitative analysis. The relative error
180 was calculated above 50% for concentrations below 0.5 wt%. The latter should thus be considered the
181 TEM-EDS detection limit and, in general, oxides concentrations below 1 wt% should be considered with
182 caution. Either photographic films (Kodak SO-163) or a slow-scan CDD camera (Olympus Tengra 2k x
183 2k x 14 bit) were used for image acquisition.
184 Electron diffraction tomography (for details on the EDT method, see Kolb et al. 2007; Mugnaioli 2015
185 and references therein) was performed with the same instrument in selected area electron diffraction
186 (SAED) mode. Two acquisitions from the same area were performed, tilting the specimen holder in steps
187 of 1 degree, respectively around the α- and β-tilt axes through the JEOL computer interface. Tilt ranges
188 for the two acquisitions were -30/+25° and -25/+17°. Precession was performed using a SpinningStar
189 precession device from NanoMEGAS and keeping the precession angle at 1°. Precession allows reducing
190 dynamical effects of electron diffraction and integrates over the whole volume of reflection intensities
191 (Vincent and Midgley 1994; Mugnaioli et al. 2009a). Diffraction patterns were acquired digitally and 3D
192 reconstructed using the ADT3D software (Kolb et al. 2011) and in-home developed routines. Reflection

intensities from the two data sets collected on the same sample area were integrated separately and merged into a single *hkl* file with no scale factor.

Cell determination was performed using the sole α-tilt data set, because the *β*-tilt reconstruction was found to be distorted, probably because the nominal tilt value does not rightly correspond to the actual sample tilt. Intensity integration, however, is not affected by *β*-tilt error. Cell parameters were subsequently refined on the basis of in-zone oriented SAED patterns acquired on the same sample after it was coated with a thin nanocrystalline Au film. The diffraction rings produced by the Au film were then used as an internal standard to rescale the data and to correct them for elliptical distortion (Capitani et al. 2006; Mugnaioli et al. 2009b; Mitchell 2015).

Structure solution was obtained *ab-initio* by direct methods as implemented in the SIR2014 program (Burla et al. 2015) employing reflections up to 0.8 Å resolution and adopting a fully kinematical approximation ($I_{hkl} \sim F_{hkl}^2$). Structure refinement was performed with the least-square method as implemented in the SHELX-97 program (Sheldrick 1997). Since electron scattering factors for Y, Nb, and W are not available, Zr scattering factors were used for Y, Mo scattering factors for Nb, and Ta scattering factors for W.

Results

Mineral association and microstructure (SEM-EDS results).

The Garnet Codera dike samples were firstly investigated by SEM-EDS techniques. SEM images with BSE detector of the polished samples reveal that they are made of aggregates of at least three different phases. EDS semi-quantitative analyses are consistent with a mineral association made of ilmenite-pyrophanite solid solution [with approximate composition $(Ti_{1.95}Fe_{1.17}Mn_{0.88})_{\Sigma=4}O_6$],

Revision 1

Hf-bearing zircon [$(Zr_{0.90}Hf_{0.07}Si_{1.04})_{\Sigma=2}O_4$], and an U-bearing phase (Figure 1a). Higher magnification images of the U-bearing phase reveal that it is pervasively zoned with two domains clearly distinct on the basis of the BSE contrast (Figure 1b).

Several spot analyses acquired in the two domains of the U-bearing phase (data not shown) revealed that the different contrast is related to substitution of (U + Th) with respect to (Y + REE), the latter more abundant in the darkest regions, in agreement with their lower mean atom weights. The compositional changes between the two domains were further investigated by EDS linescans across their interface. A representative result is reported in Figure 2. From this plot emerges clearly that moving across the interface from the brighter region to the darker grey region there is a net decrease of U and Mn and a net increase of (Y + Ta). Less palpable are a slight decrease of Th and a slight increase of Dy and Ti, whereas Nb and Fe seem roughly constant across the interface. The exchange vector that can be confidently derived at this stage is:

$$\left(\mathrm{Y + REE}\right)_{\mathrm{A}}^{3+}\left(\mathrm{Ta}\right)_{\mathrm{B}}^{5+} \leftrightarrow 2\left(\mathrm{U + Th}\right)_{\mathrm{A}}^{4+} \qquad (1)$$

However, this exchange vector is problematic, since it involves the exchange of two A-cations for one A-cation and one B-cation.

Mineral-chemistry of the U-bearing phase and radiation dose (EMP-WDS results)

Representative chemical analyses of the U-bearing phases of the Garnet Codera dike samples are reported in Table 2. Although the presence of minor hydroxyls in these minerals cannot be excluded, we assumed that low analytical totals are attributed to absorbed molecular water, a common feature of metamict minerals (Ewing 1975, Simmons et al. 2006). Since this adsorbed water is not

crystallographically bounded H_2O, atoms are recalculated on an anhydrous basis of 6 oxygens. The excess cation sums were considered for the calculation of Fe^{3+} (Droop 1987), leading to 3.0 cations p.f.u. Cation assignment to the A- and B-sites was done following Warner and Ewing (1993). Data show a quite large chemical variability, especially as regard the content of U, which appears inversely correlated with Y plus Ta. The Fe content is exceptionally high for this type of minerals, but relatively constant, as well as is Nb. Cation distribution, assuming Fe^{2+} occupying the A-site and Fe^{3+} the B-site, show a slight excess of A-site cations (Mg, Ca, Sc, Mn, Fe^{2+}, Y, Sn, REE, Th, U) and a slight deficiency of B-site cations (Ti, Fe^{3+}, Nb, Ta, W), suggesting that additional A-cations, other than Fe^{3+}, may in part occupy the B-site.

All the (Y,REE,U,Th)-(Nb,Ta,Ti) oxides reported in Table 1 fit the M:O = 1:2 stoichiometry. With the aim to classify the mineral on the basis of the chemical composition, the canonical discriminant analysis proposed by Ercit (2005) was applied. According to this classification method, the compositions of the analysed oxides, either from the darker or the brighter regions, fall in the samarskite field (Figure 3a). Further distinction within this group can be done on the basis of a ternary diagram concerning the A-site occupancy (Hanson et al. 1999). According to this diagram, the analysed samples fall in the field of samarskite-(Y) (Figure 3b). It is worth noting, however, that the (Y + REE)↔(U + Th) substitution is such to move the compositions of the brighter regions at the limit of the ishikawaite field.

According to Lumpkin and Ewing (1986), in the absence of isotope measurements, the α-decay dose of the sample can be calculated from the EMP analyses assuming the total U measured as ^{238}U and the total Th as ^{232}Th:

$$D = 8N_{238}\left(e^{t/\tau_{238}} - 1\right) + 6N_{232}\left(e^{t/\tau_{232}} - 1\right) \quad (2)$$

where N_{238} and N_{232} are the number of atoms/mg of ^{238}U and ^{232}Th, τ_{238} and τ_{232} the half-lives of ^{238}U and ^{233}Th, and t the geologic age ($25.5 \cdot 10^6$ years, Guastoni et al., in preparation). The corresponding number

of displacements per atoms (*dpa*), assuming 1500 displacements per α-decay event, can be calculated as:

$$dpa = 1500DM/N_f N_a \quad (3)$$

where M is the molecular weight in mg, N_f the number of atoms per formula unit, and N_a the Avogadro's number. From Table 2 it turns out that D ranges from $1.1 \cdot 10^{16}$ to $1.3 \cdot 10^{16}$ α-decay events/mg for areas with lower U content and darker BSE contrast, and form $1.7 \cdot 10^{16}$ to $2.2 \cdot 10^{16}$ α-decay events/mg for U richer areas with brighter BSE contrast. Corresponding *dpa* ranges are 1.3-1.5 and 1.9-2.6, respectively.

Crystallinity and crystal-chemistry (TEM-EDS results)

The structural state of the U-bearing phase as function of the U-content across the interface detected in SEM-BSE images was deeply investigated by TEM. At the TEM scale, a distinct separation between what was a clearly distinct bright-grey or dark-grey region in SEM-BSE images could not be recognised, either in terms of composition or crystallinity, but rather a continuous variation in chemical content and degree of crystallinity was found, with a great prevalence of material lacking long-range order. Indeed, bright-field images repeatedly show the spotty contrast typical of metamict materials.

Depending on the degree of radiation damage, the corresponding diffraction patterns are either typical of single crystal long-range ordered material, where the structural damage is low (Figure 4, lower line), or contain diffuse diffraction rings typical of amorphous material, where the structural damage is high (top line). Interestingly, higher resolution images acquired in these latter regions show nanoparticles with random orientation embedded within an amorphous matrix (third column). The nanoparticles probably represent a decomposition product of the radiation-induced amorphization (metamictization) process. Unfortunately, it was not possible to identify the mineral phase the nanoparticles belong to, since the error involved in the measurement of the lattice fringe distances was such that the latter could not be used

as discriminant among potential candidates – in other words, ixiolite and aeschynite with composition close to the studied system have their most "dense" lattice planes at 2.98-3.03 Å $(111)_{Ixi}$, ~2.94 $(121)_{Aes}$, and ~3.00 Å $(301)_{Aes}$, which are too close and even partially overlapped and thus impossible to be safely distinguished in high resolution images.

High-resolution images of areas with low radiation damage show that here the original crystal structure is preserved. Such crystalline areas generally have a consistent orientation over a range of several tens of nanometers, even if small lattice rotations and bending are locally observed and nanosized domains lacking of long-range order are also present. Of course, a continuous range of intermediate states between these two extremes occurs (Figure 4, second line). As expected, the degree of crystallinity is inversely correlated with the U-content (last column).

TEM-EDS results of the U-bearing phase are reported in Table 3. Each column represents the mean of several, closely spaced spot analyses representative of zones with similar degree of crystallinity, as inferred from the related SAED patterns. All the elements detected at significant level with the WDS microprobe were considered in the first round of quantification. However, only elements found always or mostly above the 2 sigma detection limit were considered in the quantification results.

Even if TEM-EDS analysis is not as accurate as WDS spectrometry – in the present case, for instance, Ti is overestimated and Ta underestimated – TEM-EDS analyses are internally consistent and some interesting hints can be inferred from Table 3. To facilitate comparison with WDS analyses, cations were normalised to 3; Fe was calculated as Fe^{2+} and entirely assigned to the A-site, along with Ca, Mn, Y, and U; Ti, Nb, Ta, and W were assigned to the B-site. In this way, an excess of A-cations and a deficit of B-cations is detected. This unbalance almost completely cancels out if part of the iron is considered oxidised, as suggested by the WDS results, and attributed to the B-sites. This hypothesis is supported by the observation that Fe does not show any clear correlation with the other cations (Fig. 5), consistent with the fact that it can be present either as Fe^{2+} in the A-site or as Fe^{3+} in the B site, thus less constrained to the

316 other cations abundances.

317 As regard the other cations, from the TEM-EDS analyses it is confirmed that U is inversely correlated
318 with Y and emerge clearly that Ti is inversely correlated with Nb (Fig. 5). The exchange vector derived
319 above can thus be tentatively refined as it follows:

320

321 $$(Y + REE)_A^{3+}(Fe)_A^{2+}(Ta)_B^{5+}(Nb)_B^{5+} \leftrightarrow 2(U + Th)_A^{4+}(Fe)_B^{3+}(Ti)_B^{4+} \quad (4)$$

322

323 This exchange vector does not consider other minor cations, namely Mg, Ca, Sc, Mn, and W, whose
324 concentration is very close or below the detection limit for the current technique. TEM-EDS, in addition,
325 cannot determine the oxidation state of some major elements, such as Fe, U, and Mn. For this reasons, the
326 above exchange vector should be considered just as a gross approximation of the real one.
327 From the comparison of the structural state as function of the U-content revealed by TEM with EMP
328 data, it can be argued that radiation doses of the order of $2.1\text{-}2.2\cdot10^{16}$ α-event/mg can make the structure
329 completely amorphous, and that crystalline domains can be hardly preserved even in areas with radiation
330 dose of the order of $1.1\cdot10^{16}$ α-event/mg, the lowest limit calculated from EMP analyses. In fact, the
331 radiation dose estimated from TEM-EDS analyses for domains that preserved the original structure (s.
332 ahead) is $0.7\cdot10^{16}$ α-event/mg at the maximum (Table 3).

333

334 **Crystallography (EDT and in-zone SAED results)**

335

336 It is well known (e.g., McLaren et al. 1994, Nasdala et al. 2006), and has been demonstrated for the
337 present case, that metamict minerals often show a striking zoning involving radiogenic elements and that
338 the original crystalline structure can be preserved in zones with lower radionuclide content. Even when
339 the bulk sample results amorphous for single-crystal and powder X-ray diffraction, these submicrometric

less-damaged domains show coherent single-crystal diffraction patterns when illuminated by electrons. Actually, conventional in-zone SAED patterns taken from coherent domains found inside the U-bearing phase of the Garnet Codera dike pegmatite have single-crystal appearance, despite some evidence of radiation-induced disorder, as ovoidal shape and splitting of the diffraction spots, caused by slight misorientation of adjoining, nanosized diffracting domains (Fig. 6). Distance and angles derived from these SAED patterns were consistent with the aeschynite-(Y) (Bonazzi and Menchetti, 1999), and considering the composition, with niobioaeschynite-(Y) (Bermanec et al. 2008).

In order to get more detailed crystallographic information about the precursor of the metamict phase, we investigated these relict crystalline areas by selected areas electron diffraction tomography (SA-EDT) (relevant data collection and refinement parameters in Table 4). The 3D diffraction reconstruction clearly shows an orthorhombic unit cell with parameter ratio $a:b:c \cong 2.1:1.5:1.0$, and extinction symbol *Pn-a*, consistent with space groups $Pn2_1a$ and *Pnma*.

In order to get accurate and precise unit cell parameters, we sputtered a thin nanocrystalline Au film on the sample and we collected a number of in-zone SAED patterns from the less damaged zones of the metamict area. Au rings were then used as an internal standard for determining the effective camera length and the elliptical distortion (Capitani et al. 2006; Mugnaioli et al. 2009b). Elliptical distortion was found to have an eccentricity of 0.22. 157 independently measured reflections were employed to refine the unit cell parameters, that eventually lead to $a = 10.804(1)$, $b = 7.680(1)$, $c = 5.103(1)$.

Reflection intensities from the EDT acquisitions were integrated and used for *ab-initio* structure determination by direct methods. Structure solution was achieved in space group *Pnma* and resulted in a model fully consistent with the structure topology of niobioaeshynite-(Y) (Fig. 7).

The structure was then refined by least-squares constraining the site occupancy to the local chemical composition obtained by TEM-EDS measurements (Table 3, column 3). Fe was distributed between the A- and B-sites in order to get rightly 1 and 2 a.p.f.u., respectively. The structural residual is quite high

because the dynamic effects could not be eliminated completely. In this respect, dynamical refinement seems a promising method (Palatinus et al. 2013; 2015), but the presence of additional problems, such as the diffuse scattering of metamict domains, that worsen the peak to background ratio, and the rotational disorder induced by mosaicity (see Fig. 6a and 6b), both affecting the correct intensity integration, discouraged us to attempt this method. The kinematical refinement, however, turned out very stable without restraints on the bond distances. The structure clearly shows the two cation sites, the 8-fold coordinated A-site, with average bond distances of 2.419 Å, and the 6-fold coordinated B-site, with average bond distances of 1.989 Å, confidently comparable with the literature data on aeschynite (Table 5). The CIF file embodying the structure factor list of the refined structure is provided as supplementary material.

Discussion

The zoning detected in the U-bearing phase of the Garnet Codera dike is unrelated with fractures in the sample (Fig. 1) and the compositional difference involved is peculiar and unrelated to what would be expected for altered samples. For instance, Tomašić et al. (2010), in a study of samarskite from Beinmyr pegmatite (Norway), found that alteration moves the composition of samarskite into the pyrochlore compositional field. Pieczka et al. (2014), in a study of samarskite group minerals and their alteration products from the Julianna Pegmatite (Poland), found that the initial stages of alteration of samarskite are characterized by a Ca-metasomatism that lead to the formation of calciosamarskite and calciopyrochlore patchy domains and eventually to the formation of secondary pyrochlore rims around samarskite. Ercit (2005) analyzed fresh and altered samarkites from REE-enriched pegmatites conserved at the Canadian Museum of Nature and concluded that the predominant effect of alteration is hydration and addition of Si and Al, moving the composition towards lower CV1 and higher CV2 values on his discriminant

canonical variable diagram, i.e., towards the pyrochlore compositional field. None of these compositional trends are involved in the zoning patterns detected in the Codera dike samples investigated in this study.

It is thus very probable that the zoning detected in the U-bearing phase is a primary growth feature, due to fast kinetic and lack of equilibrium between the growing solid and the crystallizing solution. It is suggested that the original crystal structure is preserved within zones with the lowest U-content, below ~$0.7 \cdot 10^{16}$ α-event/mg, whereas it is largely damaged up to resemble an amorphous material in the U-richest regions.

Differently from what previously presumed (i.e., Sugitani et al. 1985, Tomašić et al. 2010), our results suggest that the low temperature modification of samarskite is isostructural with aeschynite and not with ixiolite or columbite, and the structural formula is AB_2O_6 and not ABO_4 as currently accepted.

The columbite structure can be considered a superstructure of the ixiolite structure, with tripled *a* parameter, and both differ significantly from that of aeschynite, even in the powder diffraction pattern (actually there is no doubt that the calculated powder diffractogram of ixiolite matches better the experimental powder pattern obtained for the sample annealed at 550 °C in H_2 by Sugitani et al. 1984) (Figure 8). This makes difficult to reconcile our results with those of previous studies. However, it should be noted that the structure identification in previous studies was done on almost completely amorphous samples after annealing (i.e., Sugitani et al. 1984, 1985), or on the basis of few reflections on SAED patterns (e.i., Tomašić et al. 2010), which are affected by distortion and camera length (scale) fluctuation (see for instance Capitani et al . 2006; Mugnaioli et al. 2009b; Mitchell 2015), so there is a possibility that the actual crystal structure of samarskite may have been missed.

For instance, ixiolite inclusions were found within the samarskite studied here, but these cannot be considered the samarskite original structure since they are perfectly crystalline and free of radiogenic elements (Fig. 9). Thus, it is possible that ixiolite inclusions were present also the samples from Kawabe

studied by Sugitani et al. (1984), and that these inclusions could have acted as seeds during annealing leading to the ixiolite structure.

Moreover, the current TEM study has shown that the most metamict parts of the sample contain abundant nanoparticles with chaotic orientation. Even if the nature of these nanoparticles could not be determined – HR images are affected by calibration errors and astigmatism that make impossible to distinguish ixiolite than aeschynite from their lattice fringe distances and diffraction rings are too diffuse to be measured – we can reasonably assume that these nanoparticles do not represent remnants of the original samarskite single crystal, since they are randomly oriented, but rather a decomposition product of the metamictization process. Assuming that these nanoparticles have the ixiolite structure, annealing would make these particles to grow into larger domains whose presence would be finally detected in the powder diffractogram. This is similar to what observed for heavily metamict zircon, where the first steps of annealing lead to the formation of the zirconia and not of zircon, whose structure is recovered only above 1100 °C (Capitani et al. 2000).

Similarly, one could speculate that the diffraction rings used by Tomašić et al. (2010) to determine the ixiolite interplanar distances (their Table 2) could probably come from the decomposition product of the metamict processes rather than from the samarskite original structure, and the single crystal SAED pattern from ixiolite inclusions.

Finally, the comparison of the average interatomic distances of samarskite-(Y) found in the Codera dike samples with those of other minerals with Y and U as the dominant cations at the A-site and columbites, clearly shows that the crystal chemistry of samarskite fits better the aeschynite structure than the columbite (or ixiolite) structure (Table 5). Indeed, large ionic radius cations like Y and U can be better accommodated in the large A-site found in aeschynite (coordination number 8) than in the small, octahedral A-site of columbite.

Revision 1

Implications

This study plainly demonstrates that the structure of the metamict relicts with samarskite-(Y) composition found in the Garnet Codera dike have an aeschynite-like structure. This evidence raises doubts about the real structure of the samarskite mineral group, so far believed to have an ixiolite- or columbite-like structure. This inconsistency may derive from the fact that the ixiolite or columbite structure, actually detected in amorphous samples after annealing at high temperature, is the results of the recrystallization and growing of nanoparticles with ixiolite structure that form as decomposition product of the metamictization process. If this finding can be confirmed, then samarskite-(Y) and ishikawaite should be considered no longer as members of the samarskite group of minerals but rather U-rich members of the aeschynite mineral group.

These results imply that other metamict minerals such as uranpolycrase (Aurisicchio et al. 1993), samarskite-(Yb) (Simmons et al. 2006), niobioaeschynite-(Y) (Bermanec et al. 2008), calciosamarskite (Hunson et al. 1999), and possibly many other, whose identification and classification has been done on the basis of the X-ray powder diffraction on annealed samples, may hide similar pitfalls, since crystalline decomposition products of the metamict process different that the original mineral and that can growth a different phase upon annealing can be present in other mineral systems and because it has been largely documented that the recovered phase is sensitive to the annealing conditions (e.g. Sugitani et al. 1984). In this respect, transmission electron microscopy combined with electron diffraction tomography may result a valid method of investigation to validate the proper mineral specie assignment. As final corollary, this study is also the first report of the crystal structure of niobioaeschynite-(Y).

Acknowledgement

E.M. and EDT were supported by the Italian national project FIR2013 “Exploring the Nanoworld”. The authors are very grateful to the A.E. Fernando Colombo, to Greg Lumpkin and two other anonymous referees for their careful and qualified revision of the manuscript.

References

Aleksandrov, V.B. (1962) The crystal structure of aeschynite. Doklady Akademii Nauk SSSR, 142, 181-184. English translation in Doklady of the Academy of Sciences of the USSR, Earth Sciences Sections, 142, 107-109.

Aurisicchio, C., Orlandi, P., Pasero, M., and Perchiazzi, N. (1993) Uranopolycrase, the uranium-dominant analogue of polycrase-(Y), a new mineral from Elba Island, Italy, and its crystal structure. European Journal of Mineralogy, 5, 1161-1165.

Bermanec, V., Tomašić, N., Kniewald, G., Back, M.E., and Zagler, G. (2008) Nioboaeschynite-(Y), a new member of the aeschynite group from the Bear Lake Diggings, Haliburton County, Ontario, Canada. Canadian Mineralogist, 46, 395-402.

Bonazzi, P., Bindi, L., Zoppi, M., Capitani, G.C., and Olmi, F. (2006) Single-crystal diffraction and transmission electron microscopy studies of silicified pyrochlore from Narssârssuk, Julianehaab district, Greenland. American Mineralogist, 91, 794-801.

Bonazzi, P., Holtstam, D., Bindi, L., Nysten, P., and Capitani, G.C. (2009) Multi-analytical approach to solve the puzzle of a mineral from Kesebol, Västra Götaland, Sweden, belonging to the allanite-subgroup. American Mineralogist, 94, 121-134.

Bonazzi, P. and Menchetti, S. (1999) Crystal chemistry of aeschynite-(Y) from the Western Alps: residual electron density on difference-Fourier map. European Journal of Mineralogy, 11, 1043-1049.

Bonazzi, P., Zoppi, M., and Dei, L. (2002): Metamict aeschynite-(Y) from the Evje–Iveland district

(Norway): heat-induced recrystallization and dehydrogenation. European Journal of Mineralogy, 14, 141-150.

Burla, M.C., Caliandro, R., Carrozzini, B., Cascarano, G.L., Cuocci, C., Giacovazzo, C., Mallamo, M., Mazzone, A. and Polidori, G. (2015) Crystal structure determination and refinement via SIR2014. Journal of Applied Crystallography, 48, 306-309.

Capitani, G.C., Leroux, H., Doukhan, J.C., Ríos, S., Zhang, M., and Salje, E.K.H. (2000) A TEM investigation of natural metamict zircons: structure and recovery of amorphous domains. Physics and Chemistry of Minerals, 27, 545-556.

Capitani, G.C., Oleynikov, P., Hovmoeller, S., and Mellini, M. (2006) A practical method to detect and correct for lens distortion in the TEM. Ultramicroscopy, 106, 66-74.

Cliff, G. and Lorimer, G.W. (1975) The quantitative analysis of thin specimens. Journal of Microscopy, 103, 203-207.

Droop, G.T.R. (1987) A general equation for estimating Fe^{3+} concentration in ferromagnesian silicates and oxides from microprobe analyses, using stoichiometric criteria. Mineralogical Magazine, 51, 431-435.

Ercit, T.S. (2005) Identification and alteration trends of granitic pegmatite-hosted (Y,REE,U,Th)-(Nb,Ta,Ti) oxide minerals: a statistical approach. Canadian Mineralogist, 43, 1291–1303.

Ewing, R.C. (1975) The crystal chemistry of complex niobium and tantalum oxides. IV. The metamict state: discussion. American Mineralogist, 60, 728-733.

Ewing, R.C. (1976) A numerical approach toward the classification of complex, orthorhombic, rare-earth, AB_2O_6-type Nb–Ta–Ti oxides. Canadian Mineralogist, 14, 111-119.

Guastoni, A., Pennacchioni, G., Pozzi, G., Fioretti, A.M., and Walter, J.M. (2014) Tertiary pegmatite dikes of the Central Alps. Canadian Mineralogist, 52, 641-669.

Hanson, S.L., Simmons, W.B., Falster, A.U., Foord, E.E., and Lichte, F.E. (1999) Proposed

508 nomenclature for samarskite-group minerals: new data on ishikawaite and calciosamarskite.
509 Mineralogical Magazine, 63, 27-36.
510 Johnsen, O., Stahl, K., Petersen, O.V., and Micheelsen, H.I. (1999) Structure refinement of natural
511 non-metamict polycrase-(Y) from Zomba-Malosa complex, Malawi. Neues Jahrbuch fur Mineralogie,
512 Monatshefte, 1999, 1-10.
513 Kolb, U., Gorelik, T.E., Kübel, C., Otten, M.T., and Hubert, D. (2007) Towards automated diffraction
514 tomography: Part I—Data acquisition. Ultramicroscopy, 107, 507–513.
515 Kolb, U., Mugnaioli, E., and Gorelik, T.E. (2011) Automated electron diffraction tomography – a new
516 tool for nano crystal structure analysis. Crystal Research & Technology, 46, 542-554.
517 Komkov, A.I. (1965) O kristalličeskoi strukture i himičeskoi konstitucii samarskitov. Doklady Akademii
518 Nauk SSSR, 160, 693-696 (in Russian). English translation in Doklady of the Academy of Sciences of
519 the USSR, Earth Science Section, 160, 127-129.
520 Lumpkin, G.R. and Ewing, R.C. (1988) Alpha-decay damage in minerals of the pyrochlore group.
521 Physics and Chemistry of Minerals, 16, 2-20.
522 McLaren, A.C, Fitz Gerald, J.D., and Williams, I.S. (1994) The microstructure of zircon and its influence
523 on the age determination from Pb/U isotopic ratios measured by ion microprobe. Geochimica et
524 Cosmochimica Acta, 58, 993-1005.
525 Mitchell, D.R.G. (2015) Development of an ellipse fitting method with which to analyse selected area
526 electron diffraction patterns. Ultramicroscopy, 160, 140-145.
527 Mugnaioli, E. (2015): Single nano crystal analysis using automated electron diffraction tomography.
528 Rendiconti Fisici dell'Accademia dei Lincei, 26, 211-223.
529 Mugnaioli, E., Capitani, G.C., Nieto, F., and Mellini, M. (2009b) Accurate and precise lattice parameters
530 by selected area electron diffraction in the transmission electron microscope. American Mineralogist, 94,
531 793-800.

Mugnaioli, E., Gorelik, T., and Kolb, U. (2009a) "Ab initio" structure solution from electron diffraction data obtained by a combination of automated diffraction tomography and precession technique. Ultramicroscopy, 109, 758-765.

Nasdala, L., Kronz, A., Hanchar, J.M., Tichomirowa, M., Davis, D.W., and Hofmeister, W. (2006) Effects of natural radiation damage on back-scattered electron images of single crystals of minerals. American Mineralogist, 91, 1739-1746.

Palache, C., Berman, H., and Frondel, C. (1944) Dana's System of Mineralogy. 7th Edition, John Wiley, New York, 1, 797 p.

Palatinus, L., Jacob, D., Cuvillier, P., Klementová, M., Sinkler, W. and Marks, L.D. (2013) Structure refinement from precession electron diffraction data. Acta Crystallographica, A69, 171-188.

Palatinus, L., Petříček, V. and Antunes Corrêa C. (2015) Structure refinement using precession electron diffraction tomography and dynamical diffraction: theory and implementation. Acta Crystallographica, A71, 1-10.

Pieczka, A., Szuszkiewicz, A., Szełęg, E., Ilnicki S., Nejbert, K., and Turniaiak, K. (2014) Samarskite-group minerals and alteration products: an example from the Julianna pegmatitic system, Piława Górna, SW Poland. Canadian Mineralogist, 52, 303-319.

Pouchou, J.L. and Pichoir, F. (1991) Quantitative analysis of homogenous or stratified microvolumes applying the model "PAP". In Electron Probe Quantitation, Heinrich, K.F.J., and Newbury, D.E., eds., Plenum, New York, 31-75.

Sheldrick, G.M. (1997) SHELXL97: program for the refinement of crystal structures. University of Gottingen, Gottingen.

Simmons, W.B., Hanson, S.L., and Falster, A.U. (2006) Samarskite-(Yb): a new species of the samarskite group from the Little Patsy pegmatite, Jefferson County, Colorado. Canadian Mineralogist, 44, 1119-1125.

Škoda, R. and Novák, M. (2007) Y,REE,Nb,Ta,Ti-oxide (AB_2O_6) minerals from REL–REE euxenite-subtype pegmatites of the Třebíč Pluton, Czech Republic; substitutions and fractionation trends. Lithos, 95, 43-57.

Sugitani Y., Suzuki Y., and Nagashima K. (1984) Recovery of the original samarskite structure by heating in a reducing atmosphere. American Mineralogist, 69, 377-379.

Sugitani Y., Suzuki Y., and Nagashima K. (1985) Polymorphism of samarskite and its relationship to other structurally related Nb-Ta oxides with the α-PbO_2 structure. American Mineralogist, 70, 856-866.

Tarantino, S.C. and Zema, M. (2005) Mixing and ordering behavior in manganocolumbite-ferrocolumbite solid solution: A single-crystal X-ray diffraction study. American Mineralogist, 90, 1291-1300.

Tomašíc, N., Gajovíc, A., Bermanec, V., Linaríc, M.R., Su, D., and Škoda, R. (2010) Preservation of the samarskite structure in a metamict ABO_4 mineral: a key to crystal structure identification. European Journal of Mineralogy, 22, 435-442.

Tomašíc, N., Gajovíc, A., Bermanec, V., and Rajić, M. (2004) Recrystallization of metamict Nb–Ta–Ti–REE complex oxides: a coupled X-ray-diffraction and Raman spectroscopy study of aeschynite-(Y) and polycrase-(Y). Canadian Mineralogist, 42, 1847-1857.

Vincent, R. and Midgley, P. (1994) Double conical beam-rocking system for measurement of integrated electron diffraction intensities. Ultramicroscopy, 53, 271-282.

Warner, J.K. and Ewing, R.K. (1993) Crystal chemistry of samarskite. American Mineralogist, 78, 419-424.

Weitzel, H. and Schrocke, H. (1980) Kristallstrukturverfeinerungen von euxenit, $Y(Nb_{0.5}Ti_{0.5})_2O_6$, und M-fergusonit, $YNbO_4$. Zeitschrift fur Kristallographie, 152, 69-82.

Caption to Figures

Revision 1

Figure 1. SEM-BSE images of a polished section of sample 2 (sample 1 shows analogous microstructure with similar compositions). (a) Low magnification image showing the sample embedded in epoxy (peripheral black contrast). At least three different phases can be recognized on the basis of BSE contrast: ilmenite-pyrophanite, occupying the widest, dark grey area; Hf-bearing zircon, with intermediate grey contrast; and an U-bearing phase, with the brightest contrast. (b) High magnification image of the area enclosed within the black rectangle in (a) were the zoning affecting the U-bearing phase can be appreciated. A-A' trace of the linescan (see Fig. 2).

Figure 2. Representative compositional linescan across the two domains of the U-bearing phase (see Fig. 1b for locating the linescan). The linescan is composed of 103 points equally spaced within ~54 μm, each point counted for 10 s. The grey band represents the interface between the brighter (left) and the darker domain (right).

Figure 3. (a) Plot of the WDS microprobe compositions on the canonical variable diagram of Ercit (2005). CV1 = 0.106 Ca – 0.077 (Fe^{2+} + Fe^{3+} + Mn) + 0.220 Y + 0.280 (Nd + Sm) + 0.137 (Gd + Dy + Yb) + 0.100 U + 0.304 Ti + 0.097 Nb + 0.109 (Ta + W) – 12.81 (oxide wt.%); CV2 = – 0.113 Ca – 0.371 (Fe^{2+} + Fe^{3+} + Mn) – 0.395 Y – 0.280 (Nd + Sm) – 0.265 (Gd + Dy + Yb) – 0.182 U – 0.085 Ti – 0.166 Nb – 0.146 (Ta + W) + 17.29 (oxide wt.%). (b) Ternary diagrams for the samarskite group minerals. From a compositional point of view, the U-bearing phases detected in the Codera dike samples can be classified as samarskite-(Y).

Figure 4. TEM images and EDS spectra at different regions of the metamict U-bearing phase detected in the Codera dike sample. Columns are organized as to show from left to right selected area diffraction

patterns, bright field images, high resolutions images, and compositional spectra. The degree of radiation damage decreases from the top to the bottom row, corresponding to a decrease in radiogenic uranium content. Scale bar 100 nm in BF images and 10 nm in HR images.

Figure 5. Plot of the TEM-EDS chemical analyses in several areas of the U-bearing phase ordered for increasing U-content. A clear correlation among Ti, U, Ca, Ta, and Mn is observable, as well as an anti-correlation of these elements with Nb and Y. Conversely, iron does not show any clear correlation.

Figure 6. Electron diffraction experiments on crystalline areas of the U-bearing phase. (a) SAED patterns collected with $[1\bar{1}\bar{3}]$ and (b) $[10\bar{1}]$ incidence. Note the single crystal apparence but also the splitting and rotational disorder observable in high order reflections. (Indexing according to the cell determined with EDT). Reconstructed 3D diffraction space by EDT data acquisition around α-tilt, viewed along [010]* (c) and $[01\bar{1}]$* (d). Extinctions relative to the *a*-glide plane orthogonal to **c*** and the *n*-glide plane orthogonal to **a*** are marked by small arrows. (Note that these are projection of a 3D diffraction volume and not conventional in-zone 2D electron diffraction patterns).

Figure 7. Structural sketch down the **b** direction of the niobioaeschynite-(Y) as solved and refined from EDT data (**a** horizontal; **c** vertical). The structure topology, beside an origin shift, is identical to the aeschynite-(Y) refined by Bonazzi and Menchetti (1999). (Blue polyhedra = B-site; red circles = A-site).

Figure 8. Structure of ixiolite (a) and columbite (b) showing the stacking of the octahedral cations (shadowed) as seen along [001] (different colours means different cation occupancies). Note how the ordering of octahedral cations in columbite leads to the tripling of the *a* parameter, making the latter a superstructure with ixiolite subcell. Powder X-ray diffractograms of samarskite-(Y) (Sugitani et al.

1984): (c) sample annealed at 580 °C in air for 12 hrs (upon these conditions a different phase forms); (d) annealed at 550 °C for 16 hrs in H_2 (these conditions lead to the low-temperature ixiolite-like structure); (e) annealed at 950 °C for 15 hrs in H_2 (these conditions lead to the high-temperature wolframite-like structure). Calculated powder diffractograms: (f) ixiolite with cell parameters and composition of Sugitani et al. (1984); (g) aeschynite-(Y) with structure and composition obtained in this study.

Figure 9. (a) BF image showing and ixiolite crystal (ixi) making a bridge between two amorphous region of samarskite-(Y) (sam). (b) and (c) SAED patterns recorded in ixiolite along two different directions obtained rotating the crystal around **c***. (d) and (e) EDS spectra taken in the amorphous region and in the crystalline ixiolite, respectively. Note the absence of U in the latter (N.B.: the Cu peaks come from the TEM supporting-grid).

This is a preprint, the final version is subject to change, of the American Mineralogist (MSA)
Cite as Authors (Year) Title. American Mineralogist, in press.
(DOI will not work until issue is live.) DOI: http://dx.doi.org/10.2138/am-2016-5605

Table 1. (Y,REE,U,Th)-(Nb,Ta,Ti) metamict oxides relevant for the mineral association occurring in the Garnet Codera dike samples.

Mineral name	Ideal chemical formula	Space group	*a* (Å)	*b* (Å)	*c* (Å)	References
Aeschynite-(Y)	$Y(Ti,Nb)_2O_6$	*Pbnm*	5.194(2)	10.930(3)	7.386(2)	Tomašić et al. (2004)
Nioboaeschynite-(Y)	$Y(Nb,Ti)_2O_6$	*Pbnm*	5.279(3)	10.966(5)	7.443(3)	Bermanec et al. (2008)
Euxenite-(Y)	$Y(Nb,Ti)_2O_6$	*Pbcn*	14.643(2)	5.553(1)	5.195(1)	Weitzel and Schröcke (1980)
Polycrase-(Y)	$Y(Ti,Nb)_2O_6$	*Pbcn*	14.667(1)	5.593(1)	5.189(1)	Johnsen et al. (1999)
Samarskite-(Y)	$(Y,Ca,Fe)NbO_4$	*Pbcn* (?)	5.687(4)	4.925(2)	5.210(4)	Sugitani et al. (1985)
Ishikawaite	$(U,Fe,Y,Ca)NbO_4$	*Pbcn* (?)	5.664(6)	4.940(3)	5.173(7)	Sugitani et al. (1985)

Table 2. Representative WDS microprobe analyses (oxide %) of the U-bearing phases found in the Garnet Codera dike. Atom per formula unit recalculated on the basis of 6 oxygens. Cations sum to 3 a.p.f.u. after Fe^{3+} recalculation (Droop 1987). The dose (*D*, α-decay event per mg) and the related displacements per atom (*dpa*) calculated at each spot analysis are also reported. Analyses are ordered for increasing UO_2 content and distinguished on the basis of the BSE contrast.

	G4f	G4a	G4g	G4b	G4c	G4e	G4h	G4d	G1d	G1e	G1b	G1c	G1a
	Darker BSE contrast								Brighter BSE contrast				
MgO	0.14	0.09	0.08	0.13	0.07	0.07	0.16	0.13	0.10	0.12	0.10	0.12	0.11
CaO	0.31	0.37	0.42	0.41	0.33	0.38	0.26	0.24	0.26	0.18	0.28	0.21	0.21
Sc_2O_3	0.52	0.50	0.45	0.40	0.42	0.54	0.50	0.46	0.56	0.56	0.66	0.46	0.36
TiO_2	3.88	3.74	3.66	3.83	4.48	4.21	4.16	3.75	3.07	4.35	4.05	3.82	3.92
MnO	1.51	1.53	1.20	1.49	1.44	1.52	1.19	1.12	1.16	1.00	1.15	1.21	1.40
FeO	4.24	4.66	6.97	4.77	5.00	4.41	4.15	4.38	4.50	4.37	3.86	4.18	5.01
Fe_2O_3	3.55	3.10	0.37	3.03	3.10	3.72	4.58	4.74	5.03	5.32	6.06	5.48	4.16
Y_2O_3	10.70	10.50	9.90	10.16	9.89	9.98	9.97	9.77	8.33	8.91	8.95	6.93	6.60
Nb_2O_5	34.79	34.56	37.92	35.51	34.89	35.40	36.16	37.29	36.01	34.48	36.03	36.77	37.28
SnO_2	1.98	2.05	1.92	1.97	1.88	1.96	1.24	1.03	1.01	0.97	1.05	1.29	1.36
Ta_2O_5	16.93	17.23	16.71	16.53	16.90	16.78	14.03	12.59	13.74	14.57	13.13	10.35	10.59
WO_3	1.43	1.85	1.13	1.55	1.45	1.00	1.37	1.11	1.40	1.76	1.81	0.63	0.70
Nd_2O_3	0.98	1.15	0.99	1.01	1.10	1.06	1.17	0.99	1.09	1.10	1.12	1.15	1.18
Sm_2O_3	0.53	0.55	0.60	0.52	0.51	0.61	0.71	0.54	0.57	0.51	0.67	0.84	0.84
Gd_2O_3	1.60	1.35	1.44	1.60	1.12	1.13	1.15	1.12	1.10	0.88	0.98	1.18	0.98
Dy_2O_3	1.00	0.89	0.93	0.87	0.94	1.46	1.14	1.09	1.42	1.12	0.96	1.42	1.28
Yb_2O_3	0.43	0.46	0.53	0.68	0.61	0.33	0.92	0.98	0.93	0.93	1.07	0.59	0.55
ThO_2	1.29	1.63	1.32	1.59	1.45	1.41	1.28	1.36	1.43	1.54	1.59	1.66	1.75
UO_2	10.17	10.26	10.63	10.81	11.08	11.15	11.74	12.11	15.54	15.56	15.81	20.36	21.14
Total	95.98	96.46	97.17	96.86	96.66	97.11	95.88	94.80	97.24	98.24	99.33	98.62	99.41
Mg	0.015	0.010	0.008	0.013	0.007	0.007	0.017	0.014	0.011	0.012	0.010	0.012	0.011
Ca	0.024	0.028	0.031	0.031	0.025	0.028	0.019	0.018	0.020	0.014	0.021	0.016	0.016
Sc	0.032	0.031	0.028	0.024	0.025	0.032	0.030	0.028	0.035	0.034	0.039	0.028	0.022
Mn	0.090	0.091	0.071	0.088	0.085	0.089	0.071	0.067	0.069	0.059	0.067	0.072	0.083
Fe^{2+}	0.250	0.274	0.407	0.279	0.293	0.256	0.242	0.258	0.266	0.254	0.221	0.245	0.293
Y	0.400	0.393	0.367	0.379	0.368	0.369	0.371	0.366	0.313	0.330	0.326	0.259	0.246
Sn	0.055	0.058	0.053	0.055	0.053	0.054	0.035	0.029	0.028	0.027	0.029	0.036	0.038
Nd	0.025	0.029	0.025	0.025	0.027	0.026	0.029	0.025	0.027	0.027	0.027	0.029	0.030
Sm	0.013	0.013	0.014	0.013	0.012	0.015	0.017	0.013	0.014	0.012	0.016	0.020	0.020
Gd	0.037	0.032	0.033	0.037	0.026	0.026	0.027	0.026	0.026	0.020	0.022	0.028	0.023
Dy	0.023	0.020	0.021	0.020	0.021	0.033	0.026	0.025	0.032	0.025	0.021	0.032	0.029
Yb	0.009	0.010	0.011	0.014	0.013	0.007	0.020	0.021	0.020	0.020	0.022	0.013	0.012
Th	0.021	0.026	0.021	0.025	0.023	0.022	0.020	0.022	0.023	0.024	0.025	0.026	0.028
U	0.159	0.161	0.165	0.168	0.172	0.172	0.183	0.190	0.244	0.241	0.241	0.318	0.329
Σ_A	1.151	1.175	1.256	1.172	1.151	1.138	1.106	1.101	1.129	1.100	1.087	1.133	1.180
Ti	0.205	0.198	0.192	0.202	0.236	0.220	0.219	0.199	0.163	0.228	0.209	0.202	0.207
Fe^{3+}	0.188	0.164	0.019	0.160	0.163	0.195	0.241	0.251	0.267	0.279	0.312	0.289	0.219
Nb	1.106	1.100	1.195	1.124	1.103	1.112	1.142	1.187	1.151	1.085	1.115	1.167	1.180
Ta	0.324	0.330	0.317	0.315	0.321	0.317	0.267	0.241	0.264	0.276	0.244	0.198	0.202
W	0.026	0.034	0.020	0.028	0.026	0.018	0.025	0.020	0.026	0.032	0.032	0.011	0.013
Σ_B	1.849	1.825	1.744	1.828	1.849	1.862	1.894	1.899	1.871	1.900	1.913	1.867	1.820
D ($x10^{16}$)[a]	1.12	1.13	1.15	1.18	1.21	1.21	1.28	1.34	1.67	1.66	1.67	2.15	2.22
dpa[b]	1.25	1.27	1.30	1.33	1.36	1.36	1.43	1.49	1.91	1.88	1.88	2.47	2.56

[a] Dose calculated assuming the total uranium detected with the microprobe as ^{238}U and the total Th as ^{232}Th: $D = 8N_{238}\left(e^{t/\tau_{238}} - 1\right) + 6N_{232}\left(e^{t/\tau_{232}} - 1\right)$, where N_{238} and N_{232} are the number of atoms/mg of ^{238}U and ^{232}Th, τ_{238} and τ_{232} the half-lives of ^{238}U and ^{233}Th, and *t* the geologic age (Lumpkin and Ewing 1986).

[b] *dpa* were calculated assuming 1500 displacements per α-decay event: $dpa = 1500DM/N_f N_a$, where *M* is the molecular weight in mg, N_f the number of atoms per formula unit, and N_a the Avogadro's number (Lumpkin and Ewing 1986).

Table 3. Average TEM-EDS analyses (oxide %) of U-bearing phase from the Garnet Codera dike sample. Atoms per formula unit are recalculated on the basis of 3 cations. Each column refers to the average of 2-5 spot analyses carried out on closely spaced areas related to similar degree of crystallinity (the actual number of spots can be inferred from the labels). The dose (*D*, α-decay event per mg) and the related displacements per atom (*dpa*) are calculated for each average analysis. Analyses are ordered for increasing U-content.

	66-68	84-88	11-12	69-71	78-80	49-50	75-77	72-74
CaO	2.00	1.76	1.61	1.04	2.24	0.36	3.22	2.62
TiO_2	9.45	10.04	11.00	10.53	9.70	10.91	16.89	16.01
MnO	0.51	0.64	1.45	1.47	1.79	2.48	2.75	2.83
FeO	12.71	12.41	11.76	6.45	6.77	11.79	5.62	10.11
Y_2O_3	20.35	20.69	17.60	14.32	11.16	7.03	5.56	6.35
Nb_2O_5	43.72	42.45	41.57	45.52	39.56	39.00	33.76	27.70
Ta_2O_5	4.00	5.35	4.34	3.13	9.23	8.64	9.77	9.83
WO_3	5.49	3.82	3.88	3.46	5.59	2.37	2.63	3.56
UO_2	1.77	2.84	6.82	14.08	13.96	17.42	19.80	21.00
Ca	0.12	0.11	0.10	0.07	0.15	0.02	0.21	0.17
Mn	0.02	0.03	0.07	0.08	0.10	0.13	0.14	0.14
Fe	0.59	0.58	0.56	0.33	0.36	0.61	0.29	0.51
Y	0.60	0.62	0.53	0.47	0.37	0.23	0.18	0.20
U	0.02	0.04	0.09	0.19	0.20	0.24	0.27	0.28
Σ_A	1.36	1.37	1.34	1.14	1.17	1.23	1.09	1.31
Ti	0.40	0.42	0.47	0.49	0.46	0.50	0.77	0.72
Nb	1.10	1.07	1.07	1.27	1.13	1.08	0.94	0.75
Ta	0.06	0.08	0.07	0.05	0.16	0.14	0.16	0.16
W	0.08	0.06	0.06	0.05	0.09	0.04	0.04	0.06
Σ_B	1.64	1.63	1.66	1.86	1.83	1.77	1.91	1.69
D ($x10^{16}$)	0.18	0.29	0.68	1.44	1.43	1.76	2.01	2.11
dpa	0.17	0.27	0.66	1.47	1.50	1.82	2.06	2.14

Relative error (Er%) < 4 for oxide concentrations > 20 wt%; Er% < 7 for wt% > 10; Er% < 11 for wt% > 5; Er% < 20 for wt% > 2; Er% < 30 for wt% > 1; Er% < 50 for wt% > 0.5. Dose and *dpa* calculated as in Table 2, but ignoring Th.

This is a preprint, the final version is subject to change, of the American Mineralogist (MSA)
Cite as Authors (Year) Title. American Mineralogist, in press.
(DOI will not work until issue is live.) DOI: http://dx.doi.org/10.2138/am-2016-5605

Table 4. Experimental EDT data collection details and crystallographic information for the coherent crystallographic domains found inside the U-bearing phase. Two acquisitions series were performed from the same domain rotating the sample respectively around α and β tilt-axis. For cell parameters determination, only the α tilt acquisition was used. For *ab-initio* structure determination and refinement, intensities from both acquisitions were merged with scale factor 1.

System	$(Y,REE,U,Th)(Nb, Fe, Ti, Ta)_2O_6$
Tilt range α(°); β(°)	-30/+25; -25/+17
Tilt step (°)/precession angle (°)	1/1
a, b, c (Å)	10.804(1), 7.680(1), 5.103(1)
Space Group	*Pnma*
Total/ independent reflections	1570/369
Resolution (Å)/coverage	0.80/0.85
$R_{(int)}$	0.304
R_1/all	0.2795/369
R_{4s}/refl. with $F_o>4\sigma(F_o)$	0.2533/310

Table 5. Comparison of the average bond distances of samarskite (actually niobioaeschynite-(Y)) from the Codera dike with those of other minerals with similar crystal chemistry and columbites.

Phase	Sample provenance and reference	<A-O>	<B-O>	Crystal chemistry
Samarskite-(Y)	Codera Valley, Italy (this study)	2.419	1.989	$(Y_{0.53}Fe_{0.22}Ca_{0.10}U_{0.09}Mn_{0.07})$ $(Nb_{1.07}Ti_{0.47}Fe_{0.34}Ta_{0.07}W_{0.06})O_6$
Aeschynite-(Y)	Triolet Valley, Italy (Bonazzi and Menchetti, 1999)	2.388	1.973	$(Y_{0.64}REE_{0.22}Th_{0.06}U_{0.04}Ca_{0.01})$ $(Ti_{1.95}Nb_{0.05})(W_{0.03})O_{5.23}(OH)_{0.77}$
Aeschynite-(Y)	Val Vigezzo, Italy (Bonazzi and Menchetti, 1999)	2.388	1.989	$(Y_{0.65}REE_{0.16}Th_{0.07}U_{0.04}Ca_{0.01}Fe_{0.03})$ $(Ti_{1.41}Nb_{0.36}Ta_{0.22}W_{0.01})(W_{0.04})O_{5.79}(OH)_{0.21}$
Columbite-(Fe)	Minas Gerais, Brazil (Tarantino and Zema, 2005)	2.110	2.024	$[(Mn,Fe)_{0.75}Nb_{0.25}]$ $[(Mn,Fe)_{0.25}Nb_{1.65}Ta_{0.10}]O_6$
Columbite-(Mn)	Kragero, Norway (Tarantino and Zema, 2005)	2.134	2.027	$[(Mn,Fe)_{0.70}Nb_{0.25}Ta_{0.05}]$ $[(Mn,Fe)_{0.29}Nb_{1.58}Ta_{0.14}]O_6$
Polycrase-(Y)	Zomba-Malosa, Malawi (Johnsen et al., 1999)	2.373	2.014	$(Y_{0.87}Dy_{0.05}Er_{0.04}Yb_{0.02}Pb_{0.01}Th_{0.01})$ $(Ti_{1.20}Nb_{0.79}Ta_{0.02})O_{5.82}(OH)_{0.18}$
Uranpolycrase	Elba Island, Italy (Aurisicchio et al., 1993)	2.36	2.00	$(U_{0.62}Y_{0.29}Th_{0.07}Nd_{0.01}Ca_{0.02}Mn_{0.03})$ $(Ti_{1.46}Nb_{0.36}Ta_{0.12})O_6$

This is a preprint, the final version is subject to change, of the American Mineralogist (MSA)
Cite as Authors (Year) Title. American Mineralogist, in press.
(DOI will not work until issue is live.) DOI: http://dx.doi.org/10.2138/am-2016-5605

- FIGURE 1 -

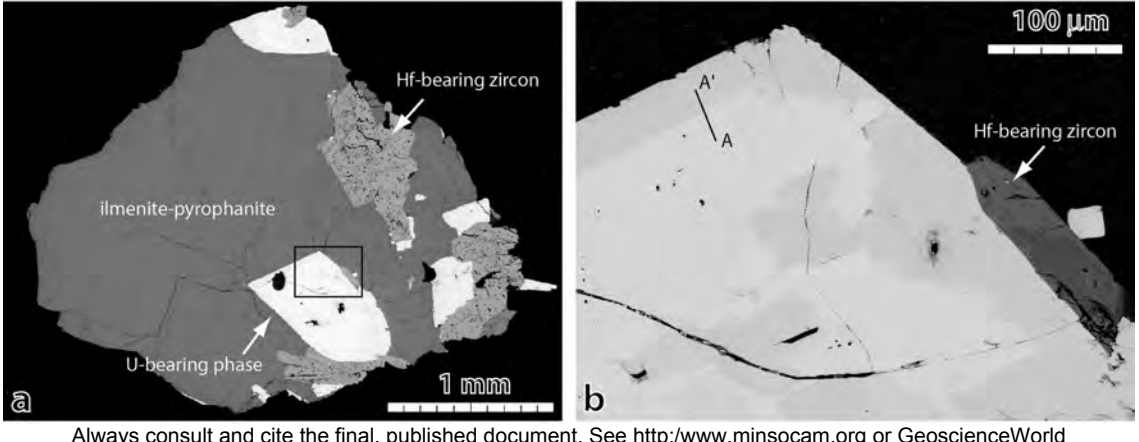

This is a preprint, the final version is subject to change, of the American Mineralogist (MSA)
Cite as Authors (Year) Title. American Mineralogist, in press.
(DOI will not work until issue is live.) DOI: http://dx.doi.org/10.2138/am-2016-5605

- FIGURE 2 -

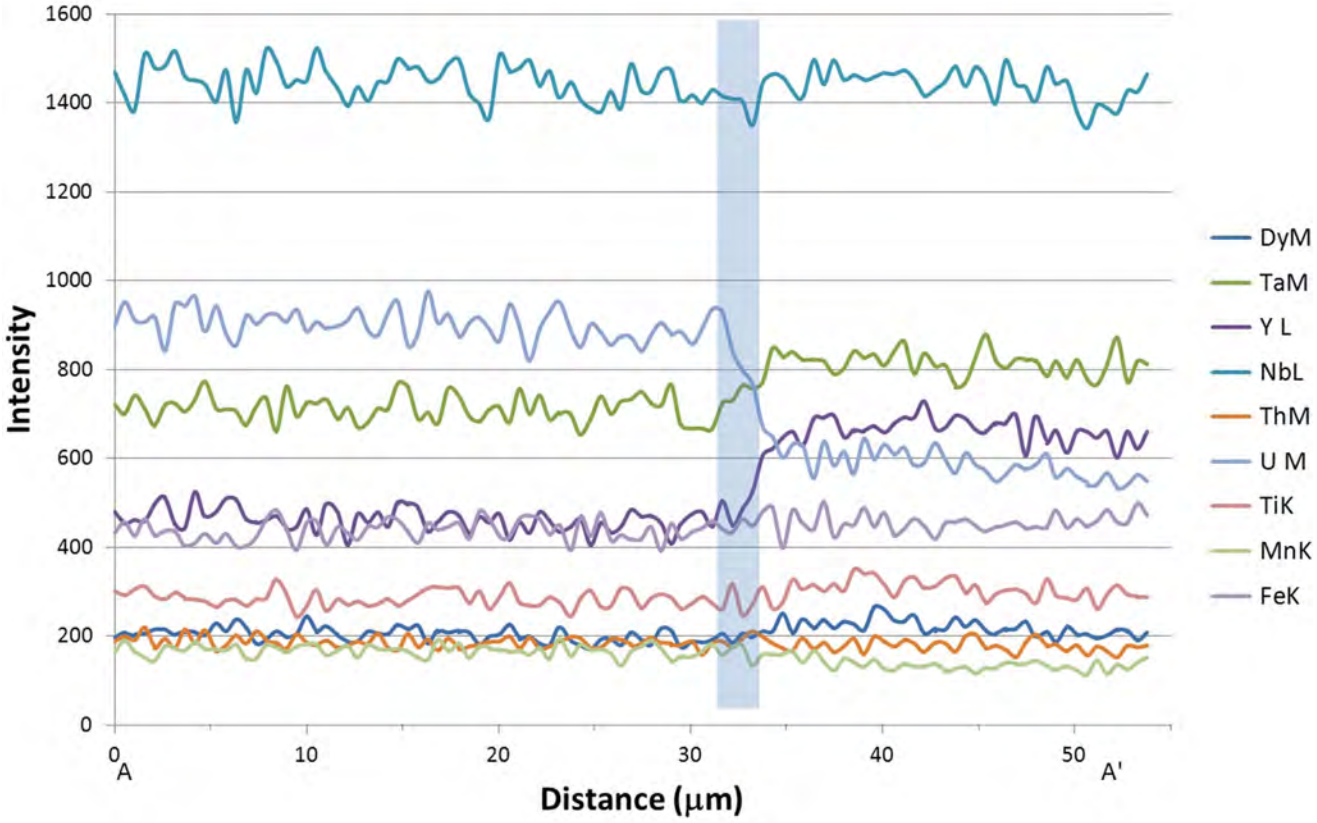

This is a preprint, the final version is subject to change, of the American Mineralogist (MSA)
Cite as Authors (Year) Title. American Mineralogist, in press.
(DOI will not work until issue is live.) DOI: http://dx.doi.org/10.2138/am-2016-5605

- FIGURE 3 -

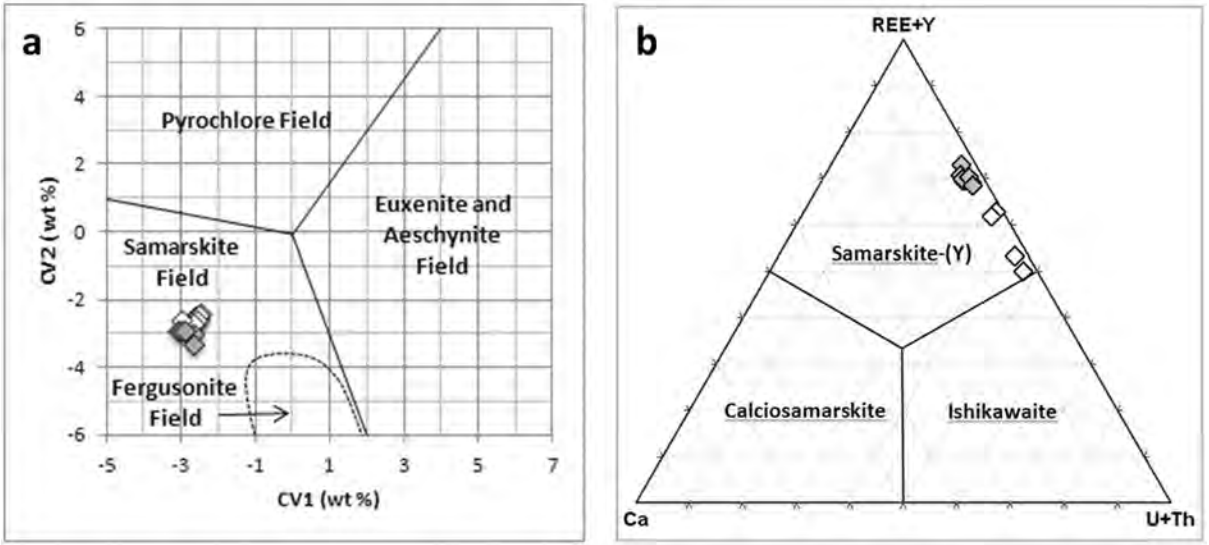

This is a preprint, the final version is subject to change, of the American Mineralogist (MSA)
Cite as Authors (Year) Title. American Mineralogist, in press.
(DOI will not work until issue is live.) DOI: http://dx.doi.org/10.2138/am-2016-5605

- FIGURE 4 -

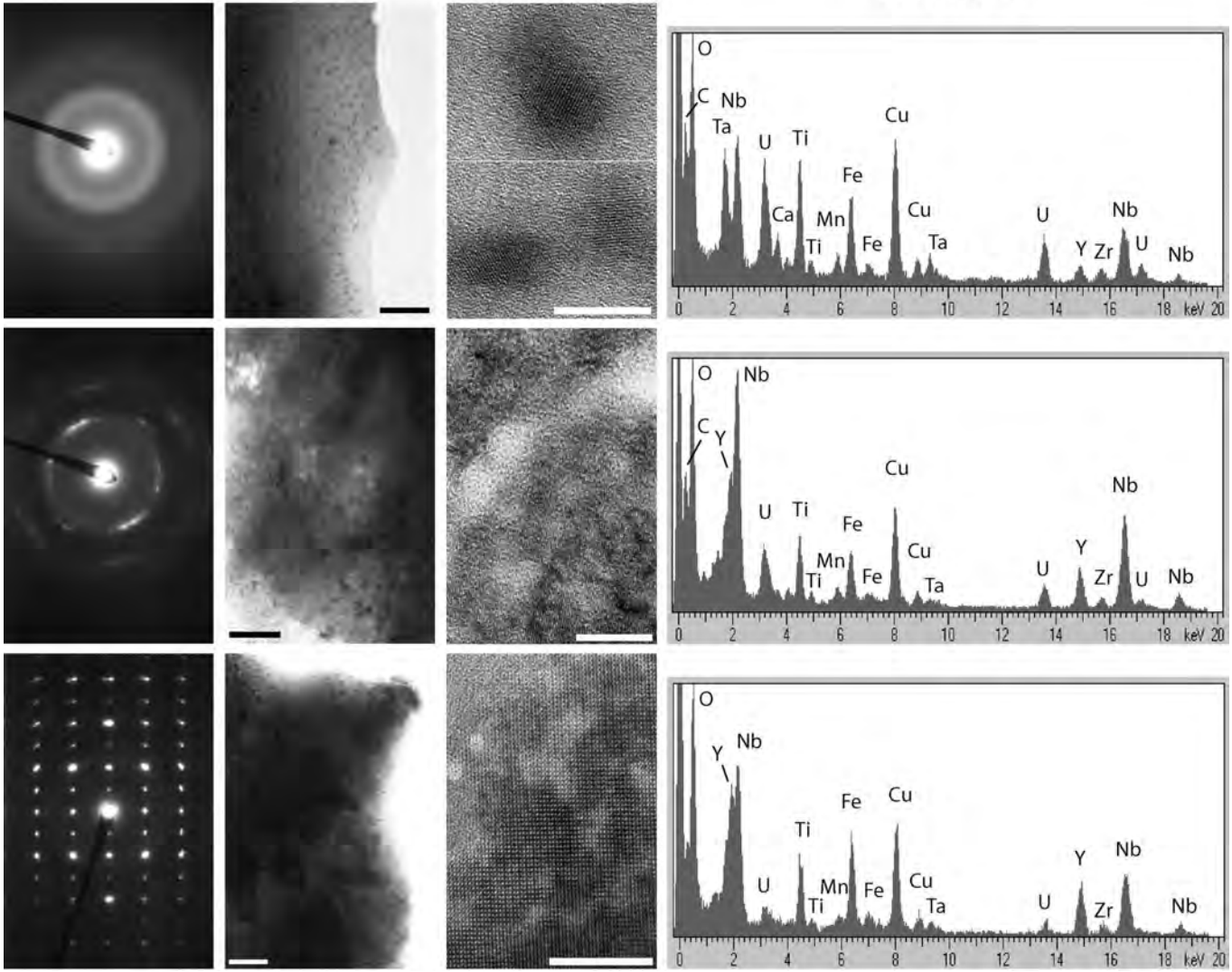

This is a preprint, the final version is subject to change, of the American Mineralogist (MSA)
Cite as Authors (Year) Title. American Mineralogist, in press.
(DOI will not work until issue is live.) DOI: http://dx.doi.org/10.2138/am-2016-5605

- FIGURE 5 -

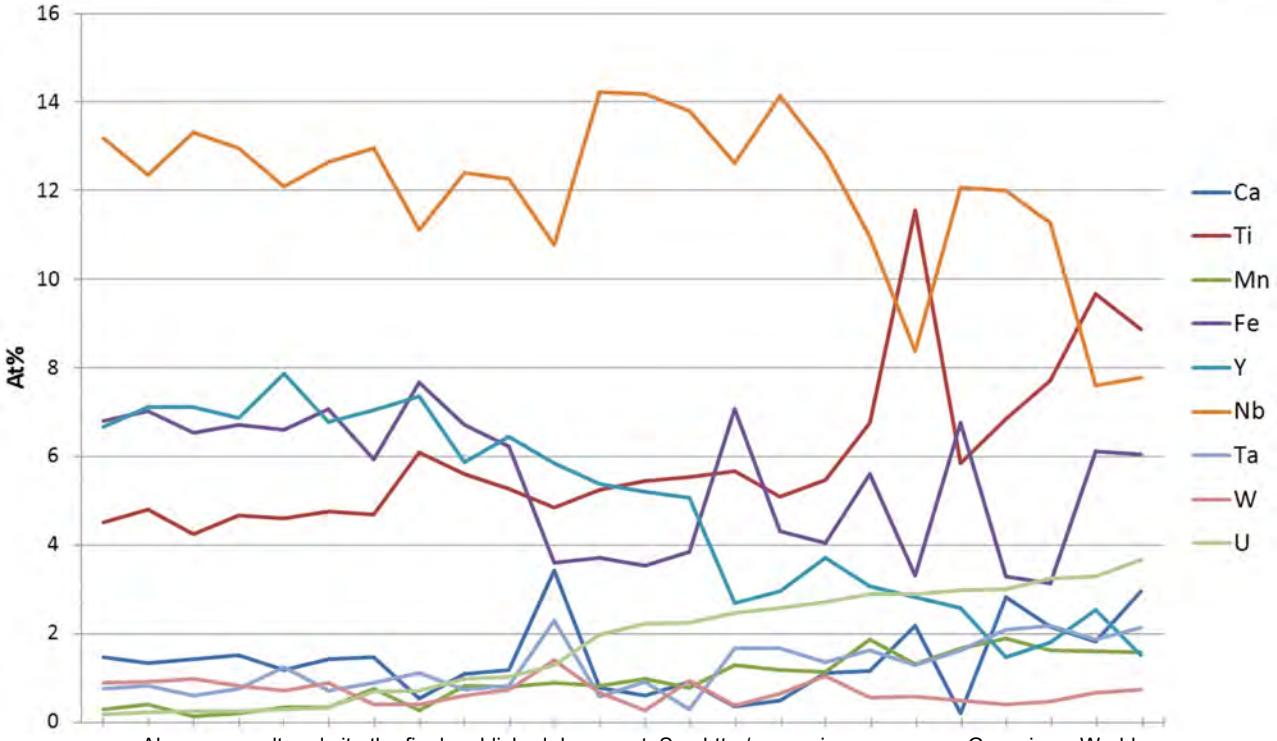

This is a preprint, the final version is subject to change, of the American Mineralogist (MSA)
Cite as Authors (Year) Title. American Mineralogist, in press.
(DOI will not work until issue is live.) DOI: http://dx.doi.org/10.2138/am-2016-5605

- FIGURE 6 -

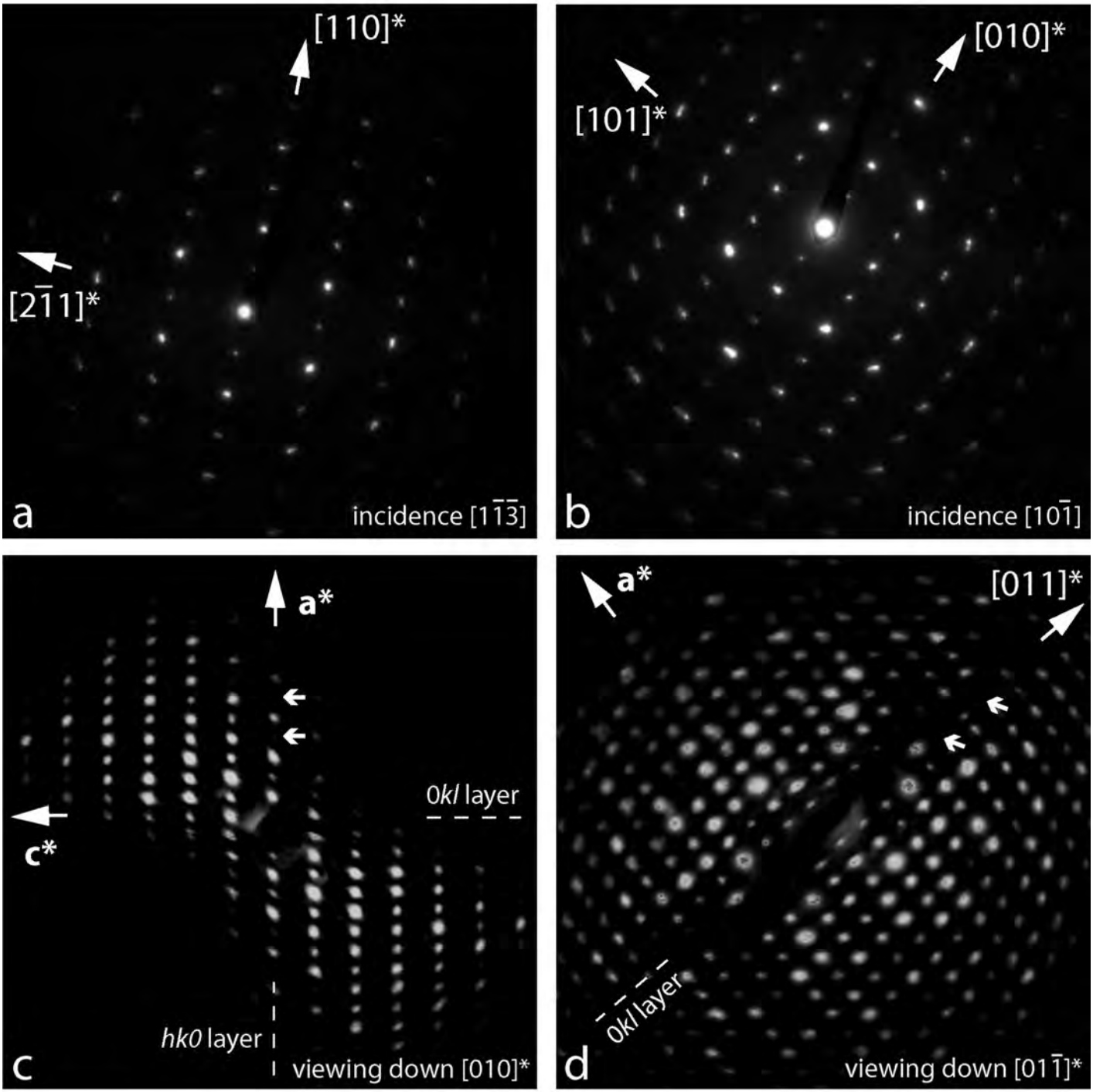

This is a preprint, the final version is subject to change, of the American Mineralogist (MSA)
Cite as Authors (Year) Title. American Mineralogist, in press.
(DOI will not work until issue is live.) DOI: http://dx.doi.org/10.2138/am-2016-5605

- FIGURE 7 -

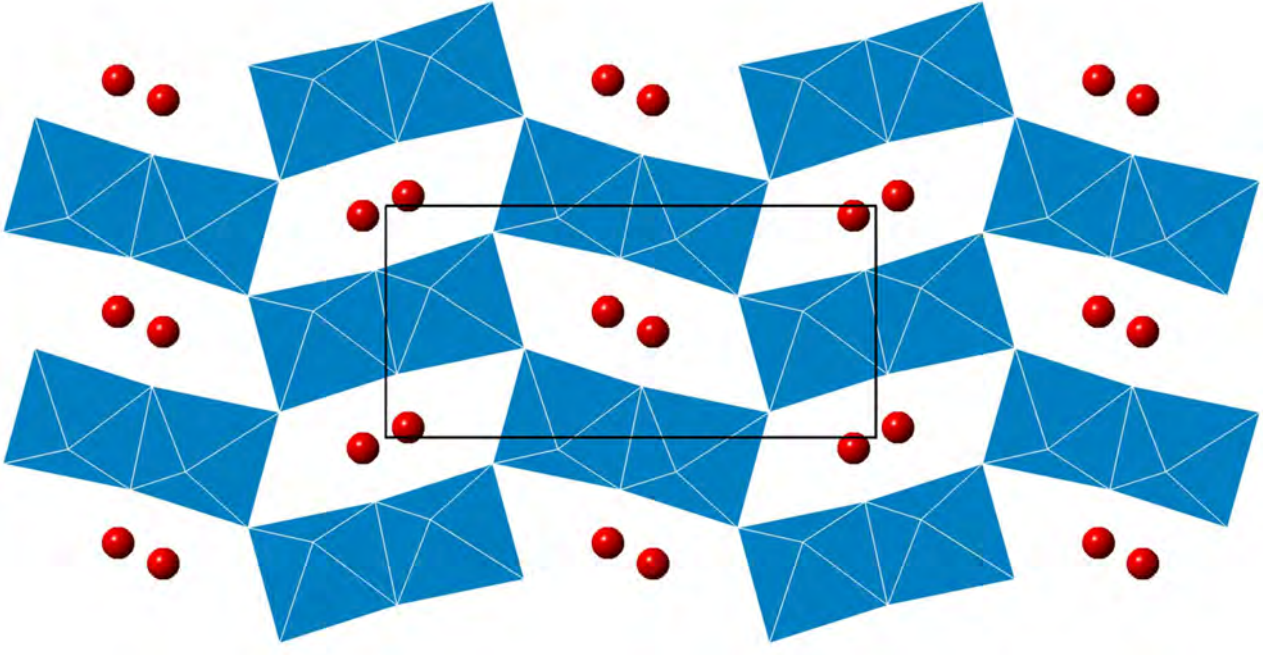

This is a preprint, the final version is subject to change, of the American Mineralogist (MSA)
Cite as Authors (Year) Title. American Mineralogist, in press.
(DOI will not work until issue is live.) DOI: http://dx.doi.org/10.2138/am-2016-5605

- FIGURE 8 -

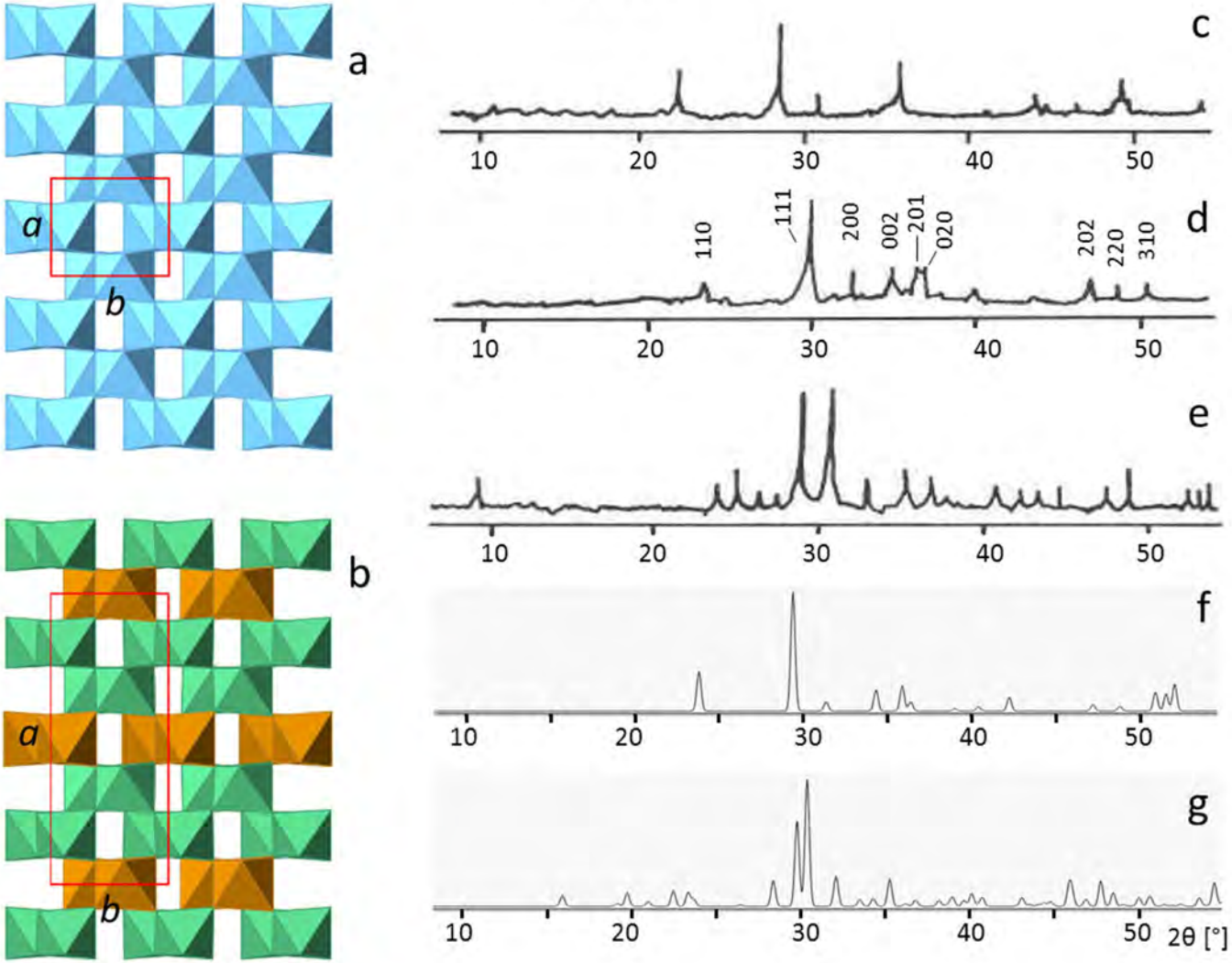

This is a preprint, the final version is subject to change, of the American Mineralogist (MSA)
Cite as Authors (Year) Title. American Mineralogist, in press.
(DOI will not work until issue is live.) DOI: http://dx.doi.org/10.2138/am-2016-5605

- FIGURE 9 -